Geochemistry, Geophysics, Geosystems

ADVANCING EARTH AND SPACE SCIENCES

RESEARCH ARTICLE
10.1029/2024GC011817

Seismic Imaging of the Reykjanes Peninsula, Iceland: Crustal-Scale Context of Geothermal Areas and Ongoing Volcano-Tectonic Unrest

J. Jenkins[1], T. Greenfield[2], R. S. White[2], J. Maclennan[2], E. Á. Gudnason[3], T. Ágústsdóttir[3], N. Rawlinson[2], A. Obermann[4], T. Dahm[5], C. Milkereit[5], A. Rahimi Dalkhani[6], J. Fone[2], G. P. Hersir[3], and J. Doubravova[7]

[1]Department of Earth Science, Science Labs, Durham University, Durham, UK, [2]Department of Earth Science, University of Cambridge, Cambridge, UK, [3]ISOR, Iceland Geosurvey, Kópavogur, Iceland, [4]ETH Departement Maschinenbau und Verfahrenstechnik, ETH Zurich, Zürich, Switzerland, [5]Wissenschaftpark Albert Einstein, GFZ Potsdam, Potsdam, Germany, [6]TUDelft, CJ Delft, The Netherlands, [7]Czech Academy of Science, Staré Město, Czechia

Key Points:

- A crustal-scale regional shear-wave velocity model of the Reykjanes Peninsula is derived from RFs and surface wave dispersion data
- Crustal thickness increases from 15 to 20 km eastwards toward the center of the Iceland Plume, due to increasing temperature/active upwelling
- Seismicity/geothermal regions are limited to the upper crust, magma is sourced from the lower crust, or a partially molten region sub-Moho

Supporting Information:

Supporting Information may be found in the online version of this article.

Correspondence to:

J. Jenkins,
jennifer.jenkins@durham.ac.uk

Citation:

Jenkins, J., Greenfield, T., White, R. S., Maclennan, J., Gudnason, E. Á., Ágústsdóttir, T., et al. (2025). Seismic imaging of the Reykjanes Peninsula, Iceland: Crustal-scale context of geothermal areas and ongoing volcano-tectonic unrest. *Geochemistry, Geophysics, Geosystems*, *26*, e2024GC011817. https://doi.org/10.1029/2024GC011817

Received 8 AUG 2024
Accepted 6 FEB 2025

Author Contributions:

Conceptualization: J. Jenkins
Data curation: T. Greenfield, E. Á. Gudnason, T. Ágústsdóttir
Formal analysis: J. Jenkins, T. Greenfield, A. Rahimi Dalkhani
Investigation: J. Jenkins
Methodology: J. Jenkins
Project administration: J. Jenkins
Resources: E. Á. Gudnason, T. Ágústsdóttir, N. Rawlinson, A. Obermann, T. Dahm, C. Milkereit,

Abstract Volcanic and seismic unrest on the Reykjanes Peninsula in SW Iceland that started in late 2019 after ~800 years of quiescence has drawn wide interest to this on-land extension of the Mid-Atlantic spreading ridge. Here, we use seismic data collected across the larger Peninsula region, covering six volcanic systems and associated high-temperature geothermal areas to produce a crustal-scale shear-wave velocity model. The model is constructed from receiver functions (RF), and pre-existing surface wave dispersion measurements from recent studies, supplemented with new inter-station paths from recent seismic deployments. We compare our velocity model to RF stacks which highlight seismic discontinuity boundaries. Results show local seismicity and geothermal systems are limited to the upper crust, which is split into an upper region of extrusive-dominated heavily fractured material <3 km and intrusive-dominated more cohesive material below. The gabbroic lower-crust is dominated by cumulates beyond 10 km depth, which are particularly high-velocity west offshore of the Peninsula. Crustal thicknesses increase from 15 to 20 km eastwards, likely reflecting increasing temperature and active-upwelling toward the center of the Iceland hotspot. Reported magma storage depths, for current and historic eruptions, generally sit within the lower-crust, but several, including for the 2021 Fagradalsfjall eruption, indicate sub-Moho storage, sourced from a seismically slow region we observe extending to 25 km, which is interpreted as representing a partially molten crust-mantle transitional region. Our seismic imaging of the Reykjanes Peninsula crust gives insight into regional crustal structure and tectonic processes, as well as providing large-scale context for the continuing volcano-tectonic unrest the region is experiencing.

Plain Language Summary Since 2019 several volcanic eruptions, and thousands of earthquakes (most too small to feel) linked to magma movement underground and near-surface cracking, have happened on the Reykjanes Peninsula in southwest Iceland, close to the capital city Reykjavik. We use large earthquakes happening 1000s of km away from Iceland, as well as ground-vibrations caused by surrounding oceans, to create images of the subsurface extending tens of km beneath this active region. Our area of analysis covers the whole of the Peninsula, including several other near-by volcanic systems and geothermal areas. We find local earthquakes and geothermal systems extend to 4–6 km, limited to the upper part of the Earth's crust. Magma feeding the current eruptions (and wider historic eruptions), mainly comes from the mid-crust (5–7 km), though some comes from deeper (>15 km) beneath the base of the crust. Our results suggest this usually solid layer (the mantle) may be partially molten here. The Earth's crust gets thicker (from 15 to 20 km) moving eastwards along the Peninsula toward central Iceland. This likely reflects higher temperatures and more mantle material moving upwards allowing thicker crust to form as you go toward a large mantle upwelling, known as a mantle plume, thought to lie beneath central Iceland.

1. Introduction

The Reykjanes Peninsula in SW Iceland forms an on-land continuation of the mid-Atlantic Ridge, accommodating divergent plate motions of 18–19 mm/yr between the North American and Eurasian Plates (Sigmundsson et al., 2020). The plate boundary (as defined by the distribution of seismicity) runs ENE-WSW along the Peninsula withlocal extension in the direction of 120°, compared to the ESE-WNW plate spreading direction of ~100–105° (DeMets et al., 2010), Figure 1—inset. This transtensional, oblique rift system runs from the off-shore

10.1029/2024GC011817

A. Rahimi Dalkhani, G. P. Hersir, J. Doubravova
Software: J. Jenkins, T. Greenfield, J. Fone
Visualization: J. Jenkins
Writing – original draft: J. Jenkins
Writing – review & editing: J. Jenkins, T. Greenfield, R. S. White, J. Maclennan, E. Á. Gudnason, T. Ágústsdóttir, N. Rawlinson, A. Obermann

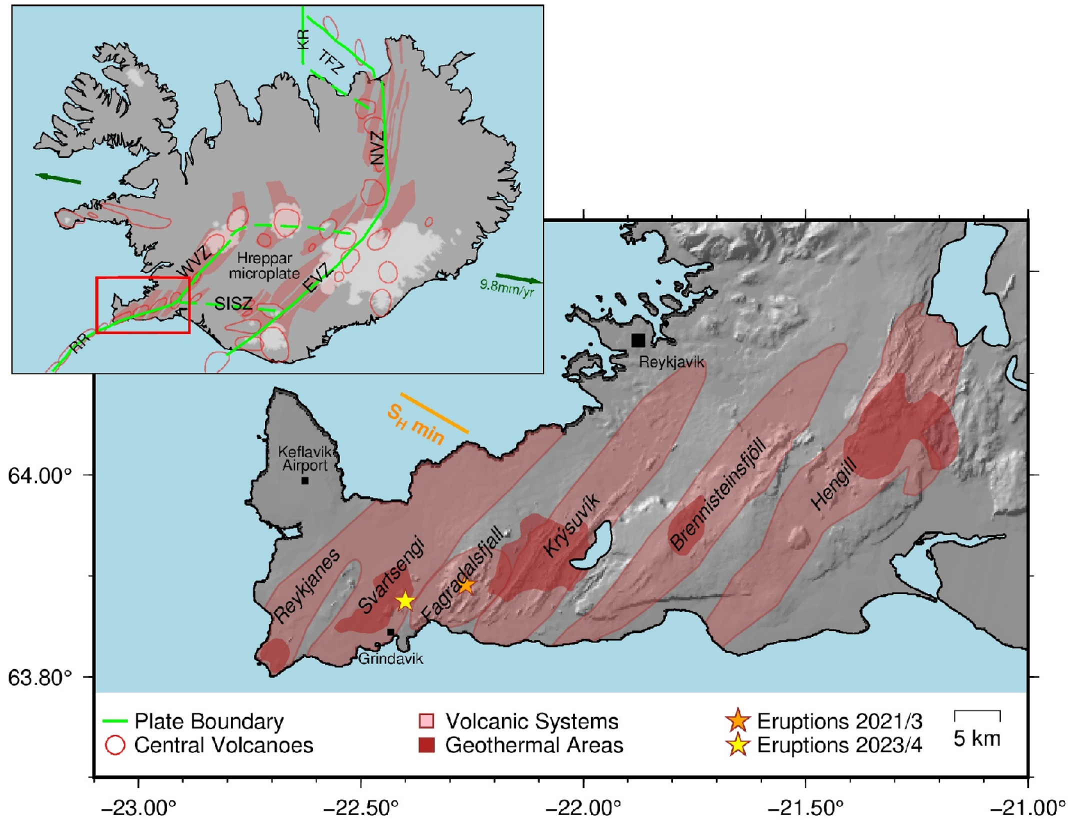

Figure 1. Map of the Reykjanes Peninsula, SW Iceland, showing the 6 volcanic systems (pink) and their associated high-temperature geothermal areas (red), according to resistivity measurements (Flóvenz et al., 2022). The approximate locations of the 2021–23 Fagradalsfjall and 2023–24 Sundhnúkar eruptions are shown as orange and yellow stars, respectively. Orientation of minimum horizontal stress (SH min) (Keiding et al., 2009) is shown with an orange bar. Inset shows the Reykjanes Peninsula (highlighted in a red box) in the context of wider Iceland tectonics. The plate spreading direction is shown with green arrows (Sigmundsson et al., 2020). Volcanic rift systems are in pink, with associated central volcanoes shown as red circles. The approximate location of the tectonic plate boundary is shown by green lines, with key segments labeled as follows: Reykjanes Ridge (RR), Western Volcanic Zone (WVZ) rift, South Iceland Seismic Zone (SISZ) transform, Eastern Volcanic Zone (EVZ) rift, Northern Volcanic Zone (NVZ) rift, Tjörnes Fracture Zone (TFZ) transform and the Kolbeinsey Ridge (KR).

Reykjanes Ridge at the Peninsula's western tip, to the Hengill volcanic system in the east, where it forms a triple junction with the South Iceland Seismic Zone (SISZ) transform zone and the Western Volcanic Zone (WVZ) rift system, which bound the Hreppar microplate.

The Reykjanes Peninsula rift system comprises six NE-SW orientated active volcanic systems. From west to east these are: Reykjanes, Svartsengi, Fagradalsfjall, Krýsuvík, Brennisteinsfjöll and Hengill (Figure 1). With the exception of Fagradalsfjall, all volcanic systems have associated high-temperature geothermal areas, with Reykjanes, Svartsengi and Hengill currently hosting geothermal power plants.

Historic volcanism over the last 4000 years has been episodic, with 400–600 years long episodes of volcanism and rifting, separated by 600–800 years of volcanic quiescence (Sæmundsson et al., 2020). In this time period, all systems experienced volcanism, except Fagradalsfjall where the most recent historic eruptions date from early Holocene, some 7000 years ago. However, in late 2019 onward, the Fagradalsfjall system started experiencing seismic unrest, dyke intrusions (Fischer et al., 2022; Sigmundsson et al., 2022) and a series of volcanic eruptions in April–September 2021, August 2022 and July 2023, on Figure 1 as orange star (Pedersen et al., 2024). These events represent the first volcanic activity on the Reykjanes Peninsula since the last major historic rifting episode ~1200–780 years before present (Sæmundsson et al., 2020). From December 2023 and continuing throughout 2024 (up to time of writing in Jan 2025), seven eruptions along with associated seismicity have occurred further westwards in the Svartsengi system (marked on Figure 1 as yellow star) just north of the town of Grindavík. These

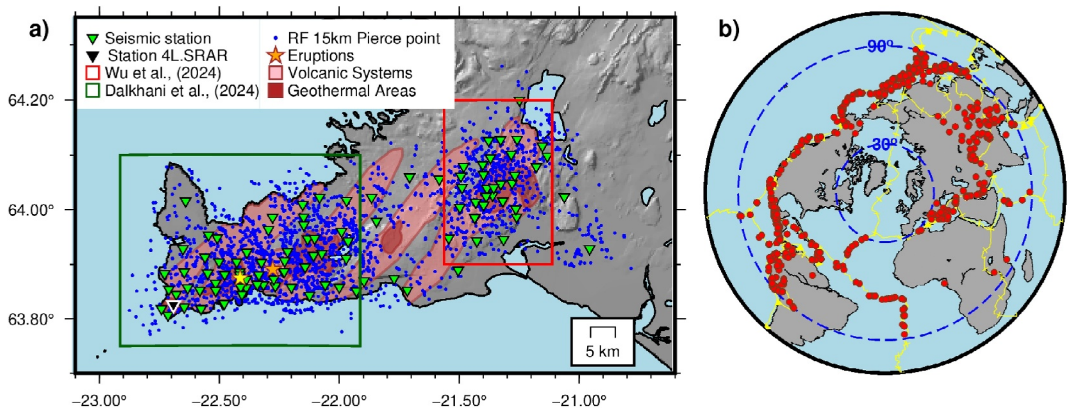

Figure 2. (a) Map showing seismic stations (triangles) used in this study (see supplementary Figure S1 in Supporting Information S1 shows these colored by network). The geographical coverage of receiver function (RF) data is shown with pierce points (blue dots), indicating where incoming Ps raypaths sample 15 km depth. The regions covered by dispersion data provided by previous studies are highlighted by colored rectangles. Tectonic features are shown as described in Figure 1. (b) Map of the 1,298 teleseismic events (red circles) used to generate RFs used in this study. Epicentral distance limits of 30 and 90° are shown with dashed blue lines, and global plate tectonic boundaries (Bird, 2003) are shown in yellow.

occupy the pre-existing Sundhnúkar crater row which was last active ~2,400 years ago (Sigmundsson et al., 2024). Based on its prior history, it has been postulated that this activity indicates that the Reykjanes Peninsula is entering a new volcanic rifting episode that may continue for several centuries (Einarsson et al., 2023).

Numerous studies have investigated crustal seismic velocity structure in different parts of the Reykjanes Peninsula, using local earthquake tomography (Obermann et al., 2022; Tryggvason et al., 2002), or surface wave dispersion methods (Málek et al., 2019; Sánchez-Pastor et al., 2021; Wu et al., 2024). However, these small-scale studies are limited in their depth resolution to less than 10 km due to the shallow distribution of local seismicity or the small distances between station pairs at which dispersion measurements can be made. The only constraints on regional scale structure down to crustal depths come from the on-land portion of the RISE active seismic refraction experiment that took place over 20 years ago (Weir et al., 2001). This provided 2D estimates of crustal thickness and a simply parameterized P-wave velocity (Vp) model along the length of the Peninsula.

In this study, we make use of the large number of seismometers that have been deployed by numerous groups across the Reykjanes Peninsula over the last 20 years to monitor geothermal areas, as well as seismic and volcanic activity (Section 2). By utilizing recordings of distant teleseismic earthquakes, constraints from previous surface wave studies and newly calculated inter-station paths, we extend imaging of shear-wave velocity structure to upper mantle depths in 3 dimensions across the whole of the Peninsula (Section 3). The results of our new velocity model (Section 4), provide insight into the depth extent of geothermal associated velocity anomalies, how crustal formation is influenced by the Iceland mantle plume and large-scale context for magma storage and ongoing eruptions and seismicity on the Reykjanes Peninsula (Section 5).

2. Data

2.1. Seismic Stations

Data from 118 seismic stations across the Reykjanes Peninsula (Figure 2a—green triangles) were used to collect a data set of global teleseismic earthquakes for analysis. All open-source data available through international datacenters as well as current and historical networks run by numerous groups were used, including data from the COSEISMIQ (Grigoli et al., 2022; Obermann et al., 2018), REYKJANET (Josef Horalek, 2013), IMAGE (Jousset et al., 2020), MAGIC (Dahm et al., 2020) and Cambridge University networks (Greenfield et al., 2022) - full details in supplementary Table S1 in Supporting Information S1, with stations colored by network shown in Figure S1 in Supporting Information S1.

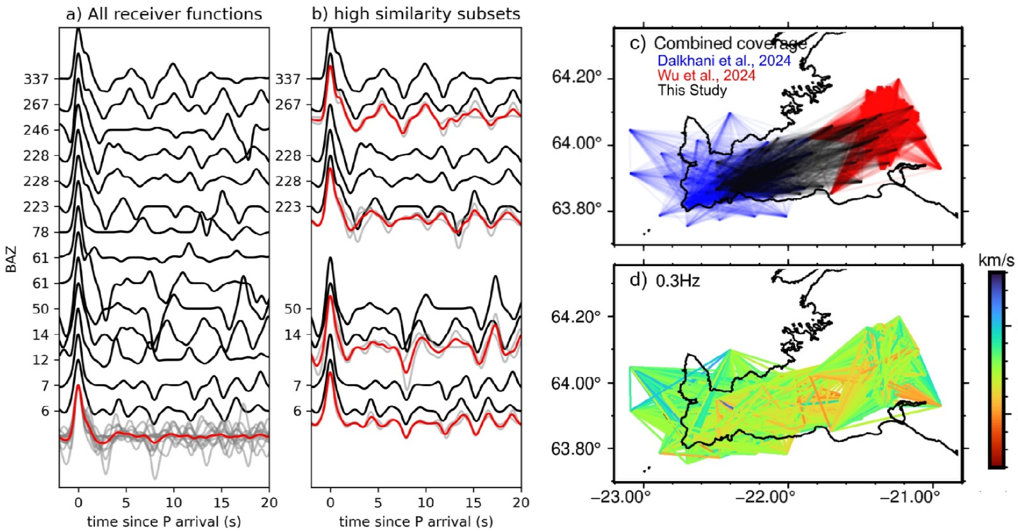

Figure 3. (a) All Receiver Function (RF) waveforms that pass quality criteria (black), plotted against back-azimuth (BAZ) for station 4L.SRAR (location shown in Figure 2). A stack of all waveforms is shown below in red, with all contributing data in gray. (b) High-similarity waveform subsets, with stacks shown in red below each group, with all contributing data in gray. (c) Geographical coverage of combined data sets of inter-station dispersion measurements, newly generated in this study (black), and provided from the studies of Rahimi Dalkhani et al. (2024) (blue) and Wu et al. (2024) (red). (d) Example of phase velocity measurements between station pairs made at 0.3 Hz used as inputs to generate regional phase velocity maps.

2.2. Earthquakes and Receiver Functions

We extract recordings from all large magnitude (>M_W 5.5) earthquakes within 30–90 epicentral degrees that occurred within the run time of each seismic station (Figure 2b) amounting to 1,298 events. Events within this distance range should contain clear P-wave arrivals, uncontaminated by mantle transition zone triplications or interactions with the outer core. Using these events, we explore compressional (P) to transverse (S) converted phases that appear within the direct P-wave coda. P-to-S (Ps) conversions are generated when seismic waves interact with sharp changes in seismic velocity. At these boundaries, some energy will be transmitted, some reflected, and some converted from P to S or vice-versa. The first 30 s after the P-wave arrival should contain direct Ps conversions generated by the crust-mantle Moho boundary (and other internal crustal interfaces), as well as multiples that are reflected or converted at layer boundaries (PPs and PSs multiples).

The small amplitude and complexity of interacting phase arrivals within the P-wave coda means that in raw seismic data, Ps phases are difficult to observe. Receiver function (RF) analysis is a common technique employed to emphasize Ps phase observations. The vertical component of motion provides a good representation of the P waveform source (for near-vertical arriving teleseismic waves), and can be deconvolved from the radial horizontal component of motion to highlight Ps arrivals of a similar shape. We use the iterative time domain deconvolution method of Ligorría and Ammon (1999), implemented within the SMurfPy Python package (Cottaar et al., 2020; Pugh et al., 2021), to produce RFs formed of a series of Gaussian peaks representing Ps phase conversions. We define a Gaussian width of 2 which imposes inherent low-pass frequency filtering of 1 Hz.

While all teleseismic earthquakes selected have the potential to generate RFs, many show no coherent signal above noise or produce unstable (e.g., "ringy") deconvolution results. Accordingly, we quality control (QC) our RF data set to produce a subset of data that can be analyzed. We use automated QC procedures defined within the SMurfPy package, followed by a visual inspection of waveforms to produce a final high-quality data set of 2,965 RFs in total.

Initial observations of RFs show highly complex waveforms that vary significantly with back-azimuth (BAZ) of the incoming raypath (Figure 3a). Specific Ps converted phases (Ps, PPs and PSs) used to analyze crustal structure are not obviously identifiable in RF waveforms. At first glance, data may appear incoherent with few clear signals that can be analyzed. However, careful manual visual inspection reveals that data recorded at a single station contains small subgroups of RFs sampling a similar region (e.g., with raypath BAZs within ~40° of each other) that show high degrees of waveform similarity up to 10–20 s after the main P-wave arrival (Figure 3b). The similarity of RFs generated by different events suggests that waveform variability does not represent noise, but complex and highly variable crustal structure. We manually identify and define 331 of these high-similarity subgroups across our RF data set for detailed analysis.

2.3. Surface Wave Dispersion Data

RF data provide good constraints on sharp seismic interfaces, but Ps phase arrival times include inherent trade-offs between the thickness and seismic velocity of imaged layers (e.g., a Ps arrival at a given time could equally represent a thick seismically fast layer, or a thin seismically slow layer). In contrast, the relationship between frequency and wave speed observed in surface waves traveling across a region (dispersion data) provides constraints on vertically smoothed absolute velocity structure. Thus, surface wave dispersion and RFs are optimal for use in joint analysis, to constrain both absolute velocity structure and sharp interfaces.

To complement our RF data set, we generate inter-station Rayleigh-wave phase velocity dispersion curves between all simultaneously recording station pairs that have been in operation since 2020 (within the University of Cambridge, REYKJANET, and COSEISMIQ networks). Daily vertical component ambient noise cross-correlation (CC) functions are computed using MSNoise (Lecocq et al., 2014), to identify Rayleigh-waves traveling between station pairs. Inter-station phase velocity dispersion curves are estimated using the real component of CC frequency spectra, following the approach of Ekström et al. (2009). Zero crossings of the spectra are modeled with a zeroth order Bessel function of the first kind, providing estimates of phase velocity (with a 2π ambiguity) at each zero-crossing frequency (see Rahimi Dalkhani et al. (2024) for detailed method description). This produces a series of potential phase velocity branches, the most realistic of which is selected based on similarity to a reference phase velocity curve (examples shown in Figure S1 in Supporting Information S1). Automatically picked dispersion curves were generated using the algorithm of Kästle et al. (2016), before being visually checked and manually re-picked where there is clear mis-selection of the optimal dispersion branch. This generated a set of 1,364 inter-station dispersion measurements (Figure 3c, black lines).

We extend our dispersion data set by integrating short period inter-station Rayleigh-wave phase velocity measurements provided by two previous studies on the Reykjanes Peninsula: Rahimi Dalkhani et al. (2024)—focused on the western Reykjanes Peninsula from Krýsuvík westwards, and Wu et al. (2024) - focused on the Hengill volcanic system (Figure 2a). This extends the geographical footprint of data coverage westwards and eastwards, along the full length of the Peninsula (Figure 3c). Dispersion data from the three studies are interpolated and resampled at common periods between 2.2 and 5 s, to provide consistent geographical coverage. Inter-station phase velocity measurements (example of 0.3 Hz data shown in Figure 3d) are used to produce regional phase velocity maps (Figure S3 in Supporting Information S1) at sampled frequencies using the Fast Marching Surface Tomography (FMST) package of Rawlinson and Sambridge (2005) - method details are provided in supplementary Text S1 in Supporting Information S1. At each station where we have RF data, dispersion curves are extracted from regional phase velocity maps. Longer period phase velocity measurements providing constraints on deeper structure are extracted from Rayleigh-wave phase velocity maps of the Iceland-wide studies of Volk (2021) between 9 and 17 s, and Harmon and Rychert (2016) between 18 and 45 s. These are combined into single pseudo-dispersion curves covering periods from 2.2 to 45 s for each station. Combined dispersion curves exhibit smoothly varying changes in velocity with increasing period, despite short and long period constraints being derived from different studies (Figure S5 in Supporting Information S1).

3. Methodology

3.1. Joint Inversion for Shear-Wave Velocity Structure

At each station, RF data in high waveform similarity subsets are inverted for shear-wave velocity structure, along with Rayleigh-wave dispersion curves (constructed as described in Section 2.3). In total, 331 highly similar subgroups are defined over 95 stations, such that 49% of the total RF data set are used in inversions (with the full data set utilized in multi-phase depth stacks outlined in Section 3.3).

We use the Computing Programs in Seismology software joint96 (Herrmann, 2013) to invert for shear-wave velocity structure using an iterative damped least squares approach. Models are parameterized with 50 1-km-thick layers, providing a model space well in excess of the theorized maximum crustal thickness in this region

(21 km suggested by Weir et al. (2001)). A constant velocity half-space of 3.8 km/s is used as a starting model for inversions, as more realistic starting models (e.g., based on local refraction experiments) were found to emphasize pre-existing velocity steps. Data is weighted 70:30 RF:surface waves, reducing the vertical averaging effect introduced when greater emphasis is placed on dispersion data. RF data is fitted up to 20 s after the direct P-wave arrival, since the latest arriving relevant multiple for a 21 km thick crust (PS20s) is predicted to occur 14 s after the direct P-wave.

The parameters described above are applied consistently for all inversions and were determined after significant parameter testing exploring the impacts on model outputs (see supplementary Text S2 and Figures S6, S7 in Supporting Information S1). Tests show that choice of starting model, depth parameterization and data weighting, produce minimal variation in the resulting shear-wave velocity models, supporting the robustness of results independent of model setup. We also explored a Bayesian inversion strategy, using BayHunter software (Dreiling & Tilmann, 2019), which was found to produce consistent results, Figure S6 in Supporting Information S1. Given similarity in outputs and the computational efficiency of a simpler iterative damped least squares approach, this was deemed a more appropriate strategy for the large data set to be analyzed.

3.2. Combining Shear-Wave Velocity Model Inversion Results

The method detailed above produced 331 individual shear-wave velocity profiles representing structure sampled by different BAZ groups at seismic stations. We combine these individual outputs into a single regional velocity model by back-projecting inverted velocity structures to depth along the raypaths of the RFs used to generate velocity profiles within a 3D grid.

A grid stretching 125 km E-W, by 84 km N-S, by 50 km in depth, sampled every 1 km in all dimensions was defined across the Reykjanes Peninsula. RF raypaths and Ps Fresnel zones were calculated for each computed velocity model, for example, the latitude, longitude location and Fresnel zone width of a Ps conversion for every depth from 1 to 50 km for each RF event used to constrain velocity models. Velocity models were then placed within the 3D grid at appropriate locations along the raypaths, across the Fresnel zone width. This introduces a small amount of lateral smoothing of structure, consistent with the data's lateral sensitivity. Where migrated raypaths overlapped, velocity models were averaged, reducing the influence of any single inversion output and allowing calculation of the standard error for each cell, based on contributing velocity model inputs. Grid cells based on averages of less than 3 velocity models were masked out, and the resulting 3D regional shear-wave velocity model is displayed as depth slices and cross-sections in the results (Section 4).

3.3. Methods Comparison: Multi-Phase Common-Conversion Point Stacking

The method detailed in Sections 3.1 and 3.2 generates velocity models which can reproduce observed waveforms. As with most inversion-based methods models are non-unique, thus to assess the validity of the structure suggested in the velocity model, we apply a second independent method directly to RF waveforms and compare the results of both approaches for consistency.

By assuming a known velocity structure, RF waveforms can be migrated to depth within a 3D grid (using the same approach applied to velocity models described in Section 3.2). However, RF waveforms contain multiple phases (both direct Pds conversions, and crustal multiples, PPpS and PsdS) each of which require a different time-depth migration. In each migration, peaks representing the target phase will migrate to the correct depth, representing a true seismic discontinuity, while peaks representing other phases will migrate to incorrect depths. To account for this, multi-phase stacking requires 3 separate depth migrations (for Pds, PPds and PSds), the results of which then only combined only where there is consistency across all 3 target phases (accounting for inverted polarities of PSds arrivals). Depth migration results in variable stretching of the waveform, thus requiring RFs be built in with different Gaussian widths, such that after depth migration the peaks are of a similar width.

On the Reykjanes Peninsula, the relatively thin nature of the crust requires narrow RF peaks for the Moho Ps phase to be visibly distinct from the preceding closely spaced P arrival. To allow for this, we rebuild our RF data set using a Gaussian pulse of $G = 6$ (equivalent to frequencies up to 3 Hz). The corresponding RF Gaussian width that produces PPds and PSds multiples of a consistent width post depth migration is $G = 2$.

We assume the velocity structure of Weir et al. (2001) (with a smoothed Moho step) along RISE line-A for depth migrations, to allow a completely independent assessment of our new velocity model. Using this, we migrate the

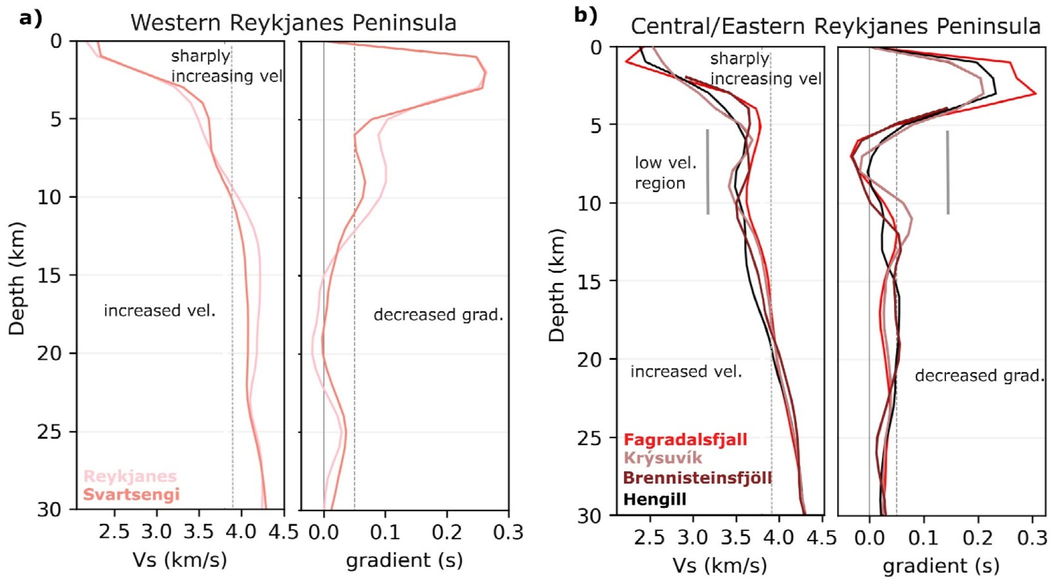

Figure 4. 1D velocity and velocity gradient profiles extracted from the 3D seismic velocity model beneath each of the volcanic systems of the Reykjanes Peninsula along the line of section shown in Figure 6. Profiles are grouped into those showing similar general structures on panel (a) the western part of the Peninsula (<−22.4° W) and (b) the central-eastern part of the Peninsula (>−22.4° W).

full RF data set to depth within three 3D grids, which are combined where amplitudes are consistent across all 3 phase arrivals. Peaks within the combined grid above 1% amplitude of the main P arrival are automatically picked to define seismic discontinuities that are compared to inverted velocity structure in our regional V_S model.

4. Results

4.1. General Velocity Structure

We observe a sharply increasing velocity with depth from the surface to approximately 4–6 km depth (which we define as the upper-crust), throughout the Peninsula (Figure 4). A P-to-s converted arrival representing a seismic discontinuity is seen within this layer at ~2–3 km depth in RF common conversion point stacks (D1 Figure 6e). Below this, structure varies between the western part of the Peninsula, including the Reykjanes and Svartsengi volcanic systems (Figure 4a), and the central-eastern part, including the Fagradalsfjall, Krýsuvík, Brennisteinsfjöll and Hengill volcanic systems (Figure 4b). In the west (Figure 4a), from 5 to 8 km depth, velocity gradients reduce and remain near constant, before a reduction in gradient around 8–10 km depth, coinciding with a gradual increase to higher velocities (> 3.9 km/s), which stabilize around 15 km depth.

In the central-eastern part of the Peninsula (Figure 4b), sharply increasing velocities in the upper-crust reach significantly higher maximum values and extend to greater depths. Beneath the upper-crust, a negative velocity gradient is observed, indicating a low-velocity region between 6 and 11 km depth. Seismic velocities then gradually increase, with gradients reaching a near constant low value between 15 and 20 km depth. Lower velocities and gradients are found at progressively greater depths moving eastwards through the volcanic systems (red-black lines in Figure 4b). This variation in velocity structure from west to east can be seen clearly in a cross-section though the velocity model shown in Figure 6, and discussed in Section 4.3.

4.2. Depth Slices and Upper-Crustal Velocity Anomalies

Figure 5 shows slices through the velocity model at depths from 2 to 7 km, colored by variation around the average shear-wave velocity at each depth, highlighting anomalous regions. High amplitude velocity anomalies are imaged at known geothermal areas; highlighted with red/blue arrows in Figure 5 and labeled by the associated volcanic system: R—Reykjanes, S—Svartsengi, K—Krýsuvík and H—Hengill. Anomalies beneath the Reykjanes and Svartsengi areas merge with each other, likely due to limiting factors of horizontal resolution. At 2 km depth, these features are observed as high-velocity anomalies, by 3 km there is a lack of clear anomalies, and by

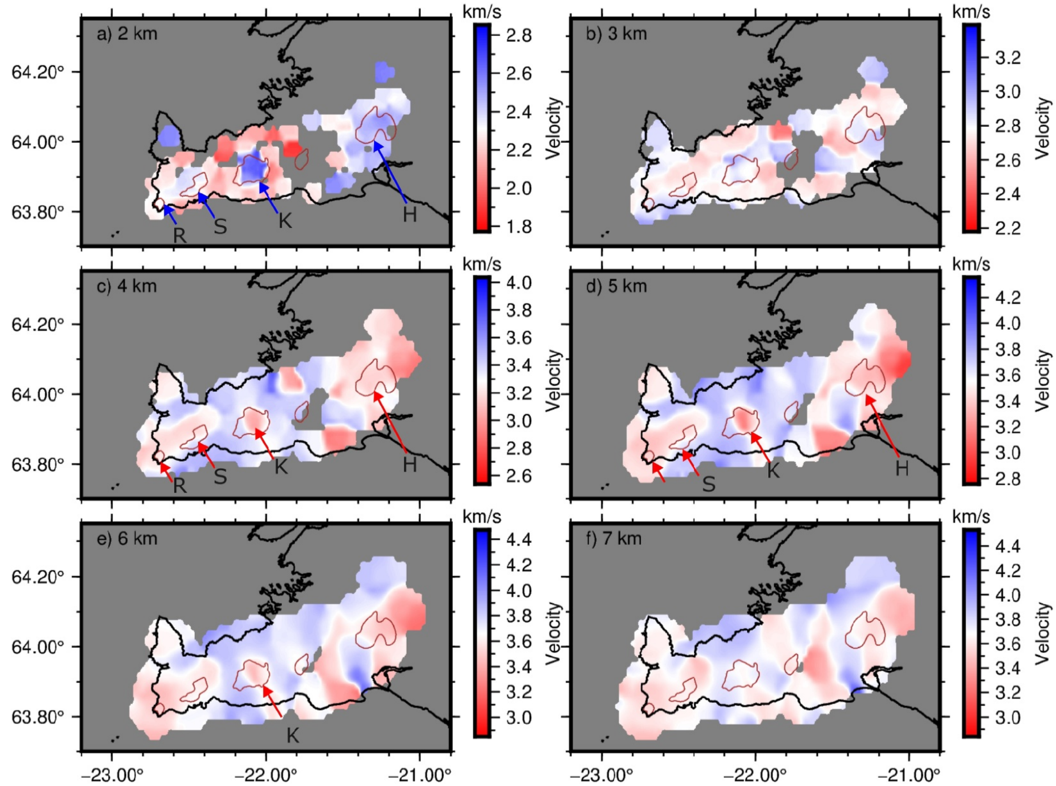

Figure 5. Maps of shear-wave velocity variation at depths of 2–7 km. Varying color scales are shown centered around the average velocity value for each depth slice. Geothermal areas are outlined in brown, with associated anomalies of note highlighted with blue (for fast anomalies) or red (for slow anomalies) arrows for the R—Reykjanes, S—Svartsengi, K—Krýsuvík and H—Hengill Geothermal areas.

4 km anomalies are observed in the same locations as at 2 km, but with the opposite polarity, now representing slow velocities. These slow anomalies persist down to 5 or 6 km depth, gradually becoming more spatially diffuse, with the most distinct anomaly in Krýsuvík (labeled K) becoming indistinct by ~7 km depth.

4.3. Lateral Variation in Velocity Structure and Crustal Thickness

Defining the thickness of the crust based on seismic velocity models is subjective, as the Moho is rarely observed as a step discontinuity, unless models have been specifically parameterized to have simple layered structures, which we have chosen not to impose. Some studies define the Moho as the point where velocities exceed a set threshold above which wave-speeds are considered more representative of mantle material (e.g., (Du et al., 2002)). Alternatively, where velocity gradients meet a set threshold can be considered (e.g., (Gilligan et al., 2015)). In stacked RF waveforms, it is often possible to define the Moho based on depths of coherent waveform arrivals (e.g., (Kind et al., 2002)). The RISE active refraction experiment identified a well-defined Moho based on PmP and SmS reflections at 14.7–20.5 km from west to east along the Reykjanes Peninsula (Weir et al., 2001), the relevant Line-A profile location is shown with a cyan line in Figure 6a. We systematically explore what combination of velocity and gradient contours that minimize the least squares depth variation between each other and the RISE Moho, to identify thresholds that can be used to map out Moho depth throughout our 3D model (see supplementary Figure S9 in Supporting Information S1). These are identified as a velocity contour of ~3.9 km/s and a gradient contour of ~0.05s^{-1}. Figures 6c and 6d demonstrate that in the central/eastern part of our model, these are consistent with RISE Moho depth estimates.

On the western part of the Peninsula and extending off-shore (<40 km along profile in Figure 6), the correlation of the RISE Moho with these contours breaks down. This coincides with a high-velocity anomaly at ~11–18 km depth (highlighted in brown in Figure 6c). The top of this anomaly is observable as an increase in velocity gradient (Figure 6d), and defined by strong discontinuity arrivals in RF CCP stacks at 11 km (D2 Figure 6e). This positive

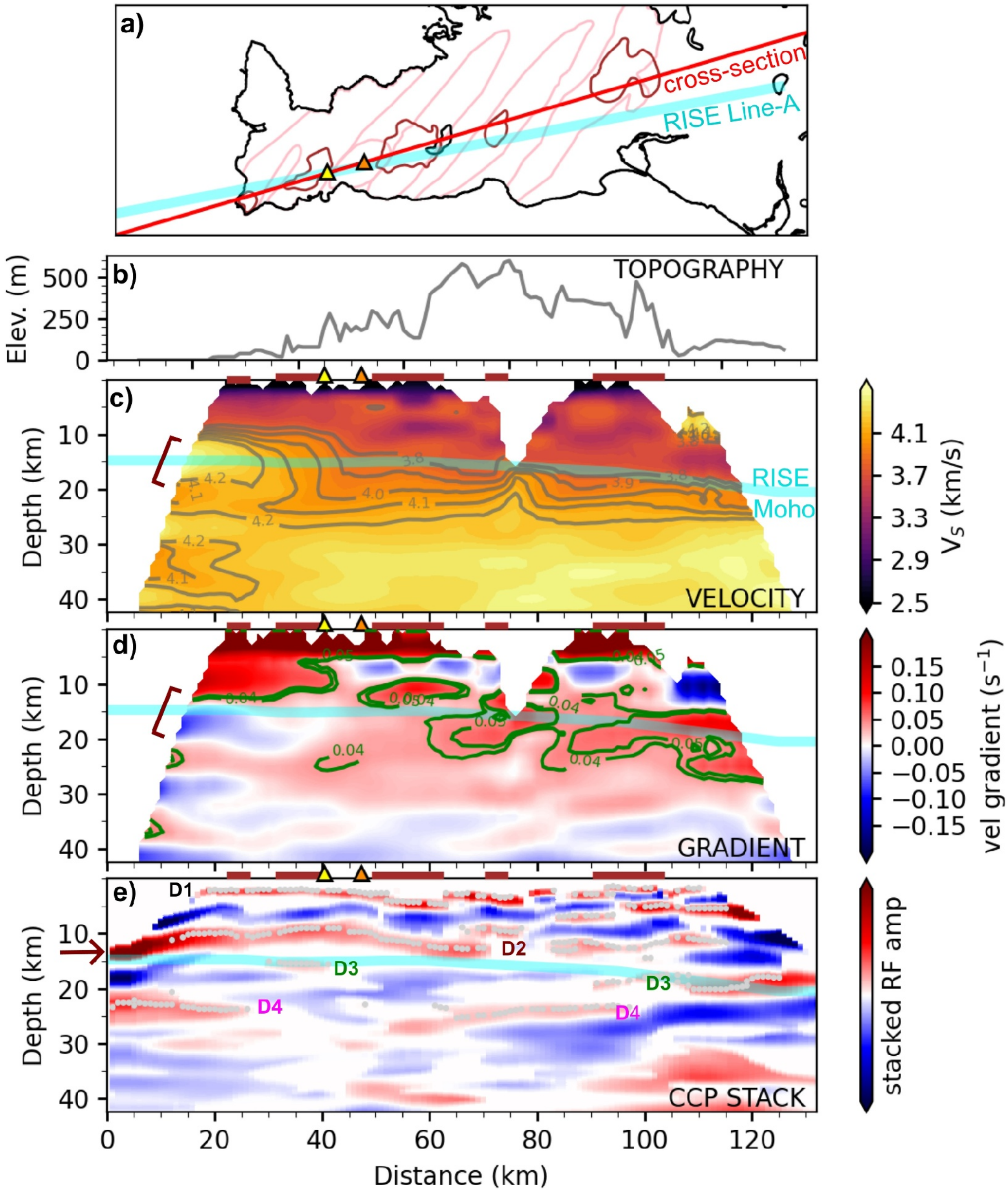

Figure 6. (a) Map showing the location of a SW-NE cross-section along the length of Reykjanes Peninsula, showing outlines of volcanic systems (pink), high-temperature geothermal areas (brown) and 2021–2024 eruption sites (triangles). Cross sections of: (b) elevation change along profile line. (c) the vs. velocity model, with 3.8–4.2 km/s contours shown in gray, (d) the vertical velocity gradients of the vs. model averaged over 5 km, with 0.04 and 0.05 s-1 contours shown in green, (e) RF waveforms combined in a multiphase common conversion point (CCP) stack, with positive peaks >1% amplitude of the main P arrival pick highlighted with pale gray points, and discontinuities of note labeled D1-D4. Predicted depths of the Moho based on the RISE refraction experiment along LINE-A are highlighted with a cyan line on all depth cross-sections (Weir et al., 2001).

velocity discontinuity (D2) extends eastwards to at least 70 km along profile varying between 9 and 13 km depth. Despite being laterally continuous, D2 is considered unlikely to represent the seismic Moho. Instead, a less obvious discontinuity in the CCP stack, D3, coincides with RISE Moho estimates (Figure 6e), but can only be seen at discrete sections along the profile (30–45 km and 90–130 km). The Gaussian pulse widths used to build RFs have a vertical resolution limit of ~5 km (Jenkins, 2017), and cannot differentiate features more closely spaced. This limit is greater than the separation between the top of the velocity anomaly off-shore west of the Peninsula, at 11 km, and estimated RISE Moho depths here (~15 km). Thus, a Moho arrival would not be

10.1029/2024GC011817

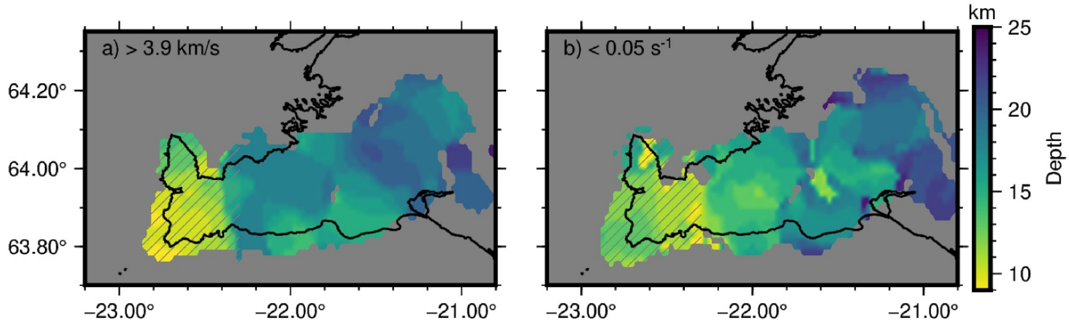

Figure 7. Maps of crustal thickness defined by (a) 3.9 km/s velocity contour, (b) 0.05 s^{-1} velocity gradient contour. Gray hatching denotes areas where these thresholds are not considered to be representative of the true crustal thickness, due to effects of an underlying lower crustal high velocity anomaly.

observable in our CCP stack here, as it would be masked by discontinuity D2. Noted sections where a discontinuity coincident with the RISE Moho are seen (D3), occur where discontinuity D2 shallows or D3 deepens, increasing the separation sufficiently to allow resolution of these two features.

Using identified velocity and gradient thresholds consistent with the Moho estimated along the RISE refraction line, we produce maps of Moho depth across the Peninsula (Figure 7). Given the high velocity anomaly in the western limit of our study region previously discussed, we only consider these reliable in the central/eastern part of the Reykjanes Peninsula (>−22.3°W). Different approaches for defining the Moho give depths that are consistent within a maximum variation of ±4 km. Irrespective of the method used to define the Moho, a thickening of the crust from west to east, from ∼15–20 km can be observed. A more subtle N-S trending saddle near −22.6°W, is coincident with a region of reduced data coverage (Figure 2a) and is thus not considered sufficiently robust to justify interpretation.

We note that the velocity threshold identified as consistent with previous RISE Moho estimates (3.9 km/s), is lower than typical mantle shear-wave velocities (~4.2 km/s). Modeled velocity values are robust (within ±0.05 km/s) independent of the value of the half space starting model used in inversions (Figure S7 in Supporting Information S1), and consistently show that more typical mantle velocities are not reached until depths of ~25 km throughout the region (Figure 6c). This also coincides with observations of weak amplitude seismic discontinuity D4 in CCP stacks (Figure 6e).

5. Discussion

An illustration summarizing our observations and their interpretation in terms of crustal structure is shown in Figure 8.

5.1. General Structure of the Upper-Crust

Sharply increasing velocity gradients that we interpret as representing the upper-crust extend to depths of 4–6 km in our velocity model (Figure 4). Within this region, CCP stacked RFs indicate the presence of a seismic discontinuity at 2–3 km depth throughout the Peninsula (D1 Figure 6e).

The upper-crust in Iceland is generally considered to be highly porous and fractured, with increasing fracture closure under lithospheric pressure and pore-space mineral infilling, explaining the increasing velocity with depth (Flóvenz & Gunnarsson, 1991). Numerous wells drilled in the Reykjanes, Svartsengi and Hengill geothermal areas support this general interpretation, showing extrusive, fractured and porous volcanic rocks in the top 1–2 km, transitioning to a mixture of intrusive/extrusive material, before reaching fully intrusive sheeted dyke complexes by 2–3 km depth (Franzson et al., 2010; Friðleifsson et al., 2017). It's reasonable to assume in most areas fluid circulation is likely to be significantly reduced within these materials, though we note that in the Reykjanes geothermal area, deep drilling suggests permeability extends into sheeted dyke complexes based on the presence of hydrothermal alteration and a total loss of fluid circulation up to ∼4.6 km as seen in the IDDP-2 well (Friðleifsson et al., 2020).

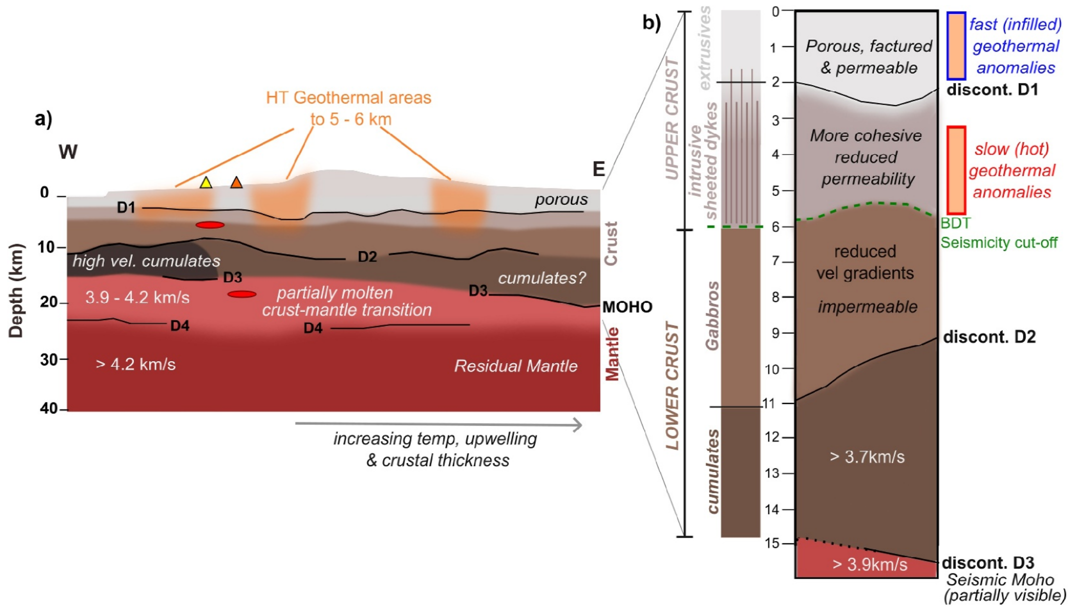

Figure 8. Summary Cartoon outlining this study's conclusions on crustal and upper mantle structure beneath the Reykjanes Peninsula. (a) Shows structural variation along a W-E cross-section along the Peninsula, while (b) highlights details of crustal structure with depth. Crustal material is shown in shades of brown, and mantle material in shades of red, where transitions between layers are based on velocity/gradient contours within our seismic velocity model or seismic discontinuities (solid black lines) observed in RF CCP stacks as described in the main text. Observations are described in normal font, and interpretations are shown in italics.

Bacon et al. (2022) show that in Iceland's Northern Volcanic zone, the majority of strong seismic anisotropy, likely caused by rift-aligned fractures, is confined to the top 3–4 km. Similarly, the recent study of Wu et al. (2024) of the Hengill volcanic system observes negative radial anisotropy ($V_{SV} > V_{SH}$), consistent with vertically aligned fractures, transitions to broadly positive anisotropy ($V_{SV} < V_{SH}$) by ~3 km. This indicates that the heavily fractured portion of the upper-crust is likely mostly confined to the more extrusive-dominated compositions, with the majority of fractures having closed by the depth predominantly intrusive compositions are reached. Thus we interpret the 2–3 km depth discontinuity D1 in RF CCP stacks as representing this transition into more coherent/less fractured, and thus seismically faster intrusive rocks (Figure 8).

5.2. Seismic Identification of Geothermal Reservoirs at Depth

All the known high-temperature geothermal areas on the Peninsula, excluding Brennisteinsfjöll, show associated velocity anomalies in the upper-crust, which transition from fast, at <3 km depth, to slow, at >3 km depth (Section 4.2). A similar observation is made by Rahimi Dalkhani et al. (2024), whose raw dispersion data contributes to our models, for the three westernmost geothermal areas: Reykjanes, Svartsengi and Krýsuvík. Rahimi Dalkhani et al. (2024) suggest that the fast shallow velocity anomalies coinciding with known geothermal areas reflect intense mineral alteration caused by circulating fluids and high temperatures which infill fractures and pore spaces, thus increasing the integrity and seismic velocity of the upper-crust. This is consistent with alteration mineral assemblages recovered from drilling of numerous geothermal wells across the Peninsula, observing mineral alteration extending to the limit of drilling, several kilometers beneath the surface (e.g., Reykjanes ~4.6 km (Friðleifsson et al., 2020; Karlsdóttir et al., 2020) and Krýsuvík ~2 km (Hersir et al., 2020)).

Beyond this depth, where we interpret a transition into an intrusive dominated and less fractured portion of the upper-crust (discussed in Section 5.1), we conclude that the dominant factor controlling velocity variation in geothermal areas becomes temperature. This explains the reversal in polarity of seismic velocity anomalies linked to geothermal systems: at shallow levels, geothermal systems represent more cohesive highly mineralized regions in the otherwise porous and fractured dominantly extrusive rocks of the shallow upper-crust (thus exhibiting faster seismic velocities). At greater depths, geothermal systems are characterized by their higher than average temperatures within the surrounding lower temperature, more cohesive intrusive rocks of the deeper portion of the upper-crust (thus exhibiting slower seismic velocities).

Our shear-wave velocity model shows that high temperatures linked to geothermal systems extend throughout the upper-crust to depths of 5–6 km. This is consistent with resistivity data from the geothermal systems of the Peninsula, which identify areas of high resistivity at depth, below a conductive cap (e.g., Reykjanes (Karlsdóttir et al., 2020), Krýsuvík (Hersir et al., 2020) and Hengill (Gasperikova et al., 2015; Árnason et al., 2010)).

5.3. General Structure of the Lower Crust and Upper Mantle

At 4–6 km depth our velocity models show a reduction in velocity gradient that we interpret as the transition into the lower crust, which is likely made up of intrusive gabbros. We see a discontinuity (D2) in the lower crust, throughout the peninsula at ∼10 km, which we interpret as representing a transition into gabbroic cumulates, where material is predominantly formed via crystal settling processes (Figure 8). At depths of 15–20 km, mostly coincident with a 3.9 km/s velocity contour (except at the western limit of the Reykjanes - discussed further in Section 5.4), we observe discontinuity D3. While this is masked in some regions (explained in Section 4.3), its consistency with the PmP reflections observed by Weir et al. (2001), suggests this represents the seismic Moho.

Velocities of 3.9 km/s found at Moho depths, are lower than typical mantle velocities (∼4.2 km/s), which are not reached in our models until consistent depths of ∼25 km beneath the Peninsula, coincident with discontinuity D4 (Figure 8). The region from 15/20–25 km beneath the seismic Moho, we interpret as representing a thick partially molten transitional zone between the crust and underlying residual mantle, comprising solidified cumulate gabbros, high melt fraction sills, and some interstitial melt—in a background of olivine-rich material, such as peridotites and ultramafic cumulates. This would be similar to the lower-most layer in ophiolite sequences, usually referred to as the Moho Transition Zone (Korenaga & Kelemen, 1997), though this is observed to be reasonably thin (10–100s m), with maximum thicknesses overlying regions of upward mantle flow (Boudier & Nicolas, 1995). Under slow spreading ridges, Cannat (1996) propose a crustal model which includes a significantly thicker layer of similar material (possibly up to 5 km), which they describe as extensively tectonized upper mantle rocks, formed of intrusive primitive gabbros, ultramafic cumulates, and variably impregnated ultramafic rocks. With plume influenced spreading, occurring above sea level, Iceland is not representative of typical mid-ocean ridge spreading settings. We hypothesize that higher temperatures and plume-linked upwelling, in addition to slow effective spreading due to the distributed nature of rifting across the en-echelon volcanic centers on the Reykjanes Peninsula, could produce a thickened Moho-transition zone style layer here.

5.4. Western Reykjanes High Lower Crustal High Velocity Anomaly

We estimate crustal thickness partially based on a velocity threshold of 3.9 km/s. If this definition of Moho depth is extended to the western limit of the Reykjanes peninsula, it would suggest crustal thicknesses of only 10 km in this region. This is inconsistent with previous studies that suggest thicknesses' of 14–15 km here (Rahimi Dalkhani et al., 2024; Weir et al., 2001), with thicknesses of ∼10 km not being observed until >160 km SW off-shore along the Reykjanes Ridge (Smallwood & White, 1998; Weir et al., 2001).

It is more likely that in this area, this velocity threshold ceases to be representative of the Moho due to the high velocity anomaly observed between ∼11–18 km depth (Figure 6c). The top of this feature is defined by discontinuity D2 in CCP stacks at 11 km (Figure 6e), which we suggest masks signals from the underlying Moho (see Section 4.3). Weir et al. (2001), note a lower crustal reflector in this region on LINE-A of the RISE refraction experiment, which is seen as a step increase in Vp velocity (by up to +0.5 km/s) at 9–11 km depth, over several km laterally. The authors postulate this represents lower crust heavily intruded with ultra-mafic cumulates. Discontinuity D2 defines the top of the feature (illustrated in Figure 8), but extends further eastwards beyond the high velocity anomaly itself. If this discontinuity marks a transition into a cumulate dominated lower-most crust throughout the Peninsula as we interpret, this leaves the question of why cumulates at the western limit show significantly higher velocities than elsewhere.

It is notable that the plate boundary bends eastwards moving from offshore to onshore, becoming significantly more oblique at approximately this location. This change in orientation may be linked to the eastwards migration of the dominant spreading center via a rift jump eastwards into the EVZ, following hypothesized eastwards migration of the underlying mantle plume (Harðarson et al., 2008). This could lead to a scenario where melt

10.1029/2024GC011817

accreting at the rift bend is intruded into older and colder crust at this location. As noted by Weir et al. (2001) this would lead to less remelting and crustal assimilation, potentially allowing more enriched cumulates to settle out.

5.5. Variations in Crustal Thickness

We observe an increase in crustal thickness (∼15–20 km) moving from west to east across the Reykjanes peninsula, consistent with previous studies. An eastwards thickening trend (14–20 km) was noted in the RISE refraction study of Weir et al. (2001), and Bjarnason et al. (1993) observed thicknesses of 21 km just beyond the eastern limits of our study area in the SIST refraction experiment.

Weir et al. (2001) interpret this increase in crustal thickness as a direct result of increasing mantle potential temperature moving toward the center of the Iceland mantle plume core, situated beneath central Iceland. Using theoretical predictions of oceanic igneous thickness as a function of mantle potential temperature (following the approach of Parkin and White (2008)), if increased passive upwelling with higher temperature under the spreading center is assumed to be the sole cause of the 5 km increase in crustal thickness, this requires a relative mantle temperature increase of ∼50–65°C eastwards along the Peninsula.

This would represent a large proportion of the total temperature excess estimated at the center of the Iceland plume several hundred degrees (Allen et al., 2002; Ito et al., 1999; Maclennan et al., 2001; Matthews et al., 2021), occurring over the reasonably short distance of the Reykjanes Peninsula. Increased melt production leading to thickened crust could theoretically also be driven by increasing plume-driven active mantle upwelling, or increasing mantle fertility. Though Shorttle et al. (2013) showed that melts with increased amounts of fusible material didn't have a significant effect on crustal thickness in Iceland.

Kelemen and Holbrook (1995) argue that the relationship between lower crustal velocity and crustal thickness can aid in differentiating between these mechanisms. Analysis of average lower crustal velocities shows increasing velocity with increasing crustal thickness (full details in supplementary Text S3 and Figures S10 and S11 in Supporting Information S1). This relationship is suggested by Kelemen and Holbrook (1995), to be inconsistent with an increasing mantle fertility mechanism, and instead supports increased mantle temperatures allowing deeper melt generation, leading to compositions more enriched in Mg/Fe which produce higher velocity lower crust. Increased active upwelling, would not significantly alter melt compositions/lower crustal velocities, so cannot be ruled out as a contributing factor based on this analysis.

However, we note there is a lack of petrological trends in erupted materials moving from west-east across the region, supporting an interpretation of increasing mantle potential temperature. Caracciolo et al. (2023) observe a slight increase in K_2O/TiO_2 ratios of erupted products moving eastwards, based on analysis of samples from volcanic groundmass glass from the last rifting episode on the Reykjanes Peninsula - the 800–1240 CE Fires. This indicates a decrease in melt fraction - the opposite of what would be expected for increasing mantle potential temperatures. Increased melt production driven by an increase in active plume-driven upwelling, however could be consistent with increasing K_2O/TiO_2 ratios. If active upwelling is also a contributing factor to increasing crustal thicknesses, this would require more modest temperature increases over the limited distance of he Peninsula, thus it seems likely that a combination of these mechanisms contributes to the increasing in crustal thicknesses we observe.

5.6. Relationships Between Final Magma Storage Depth and Crustal Structure

Olivine-Plagioclase-Augite-Melt (OPAM) barometry can be used to draw conclusions about final depths of magma storage. Reasonably consistent storage depths are found along the majority of the Reykjanes (7–10 km beneath Reykjanes/Svartsengi/Krýsuvík volcanic systems), by Caracciolo et al. (2023) based on OPAM analysis of samples from lava units from the last rifting episode. Our results suggest these magma accumulations would lie toward the top of the lower crust, above what we interpret as the cumulate dominated lower-most crust. Caracciolo et al. (2023) show notable exceptions in the Brennisteinsfjöll volcanic system, where melts appear to be sourced directly from deeper reservoirs (14–21 km), consistent with our interpretation of this depth range representing a partially molten crust-mantle transitional zone.

Baxter et al. (2023), analyzed a countrywide compilation of OPAM data from across Iceland compared to calculations of magma flux (based on multiplication of crustal thickness and spreading rate, over rift zone area). This revealed long-wavelength correlations of decreasing storage depth with increasing magma flux (generally linked

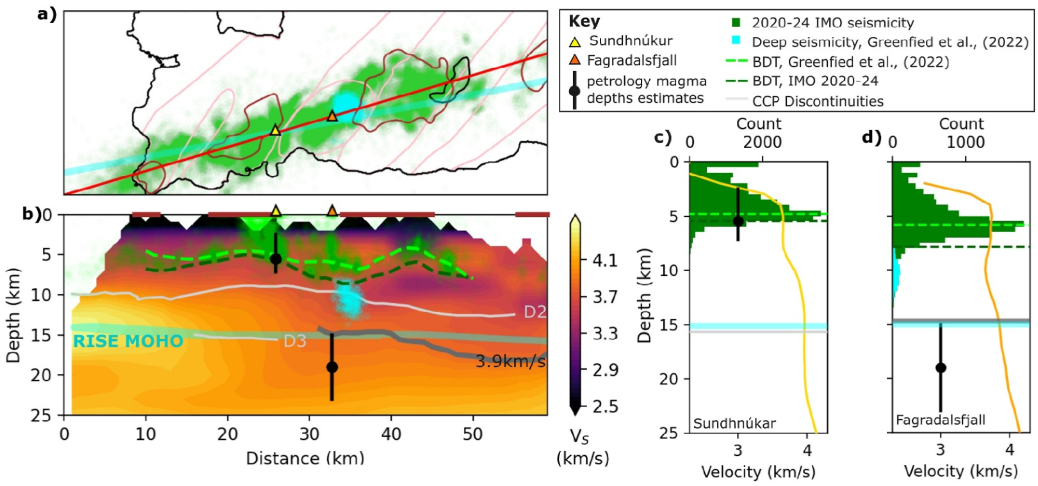

Figure 9. Local seismicity and estimates of magma storage depths from the period of volcanic unrest on the Reykjanes Peninsula between 2020 and 2024 (as labeled in legend top right), in the context of our crustal velocity model. (a) The location of cross-section through our Versus velocity model shown in b, as a red line, and location of the RISE refraction experiment LINE-A as a cyan line (Weir et al., 2001), along with eruption sites and IMO seismicity. (b) Cross section through our velocity model, and seismic discontinuities seen in RF CCP stacks, compared to depth extent of seismicity occurring within 1 km of section. Estimated Brittle-Ductile Transitions (BDT) shown as dashed lines, and depth of estimated magma storage shown as red/brown points/crosses. (c) and (d) show extracted velocity profiles beneath the Grindavík/Sundhnúkar and Fagradalsfjall eruption sites (yellow and orange triangles on panels (a and b) respectively.

to thicker crust), which they hypothesize reflects the influence of increased crustal thickness on thermal structure, allowing stabilization of shallower magma storage. We note this trend is not seen on the Reykjanes—where an eastwards increase in crustal thickness, does not correlate with shallowing magma storage. In a recent extension of this work, Baxter and Maclennan (2024) show this relationship also holds-true offshore, west of our study region along the Reykjanes Ridge, suggesting the Reykjanes Peninsula represents an anomalous region in this otherwise reasonably consistent trend. However, this area represents a more complex 3D spreading scenario than the majority of rift systems both onshore and off-shore Iceland. Distributed spreading in this transtentional setting, which is made up of a complicated arrangement of en-echelon volcanic systems, will inevitably lead to uncertainty in estimates of rift zone area and the calculated magma flux rates used to define these relationships, perhaps explaining the breakdown of correlation in this region.

5.7. Crustal Context of Ongoing Seismic and Volcanic Unrest

Using our new crustal velocity model, we provide large-scale context for the recent volcanic eruptions on the Reykjanes Peninsula, including the 2021–23 Fagradalsfjall eruptions and the 2023–24 Sundhnúkar eruptions near Grindavík, Figure 9.

5.7.1. Seismicity

Both eruptions and associated dyke intrusions not resulting in magma reaching the surface have been accompanied by variable amounts of seismicity linked to deformation and subsurface magma movement (De Pascale et al., 2024; Fischer et al., 2022; Greenfield et al., 2022; Parks et al., 2023; Sigmundsson et al., 2022, 2024). The most temporally complete record of seismicity is captured by the regional seismic network in Iceland (SIL), operated by the Icelandic Meteorological Office (IMO). The IMO catalog (Icelandic Meteorological Office, 1992) is displayed in Figures 9a and 9b in both map view and depth cross-section, for events recorded between January 2020–March 2024. Using the IMO catalog, we calculate the Brittle to Ductile Transition (BDT) as the depth above which 90% of all seismicity lies—marked as dark green dashed line in Figure 9b. Below this depth, it is assumed that higher temperatures inhibit brittle deformation, resulting in the sudden drop in seismicity. The IMO based BDT lies at ~6–8 km depth, just below the base of the sharply increasing velocities we use to define the upper-crust (Figures 9c and 9d).

While the IMO catalog provides the most complete record of seismicity throughout this period, the accuracy of event locations, particularly in terms of depth, is likely to be poorly constrained due to a lack of directly overlying seismic stations. In comparison, the catalog of Greenfield et al. (2022) is more temporally limited (covering only the period around the first eruption at Fagradalsfjall: June 2020 - August 2021), but likely provides more accurate depth estimates, due to a dense overlying network of stations and use of a region-specific local velocity model derived from event picks. Estimates of the BDT based on the Greenfield et al. (2022) catalog (bright green dashed line Figure 9) is several km shallower than the IMO based BDT, falling at ∼5–6 km depth, and aligning more directly with where we identify the base of the upper-crust.

The correlation of the seismic BDT with the base of the upper-crust is consistent with an interpretation of decreasingly porous and fractured rock with increasing depth. Laboratory observations show that decreasing porosity is linked to increasing thermal conductivity (Mielke et al., 2017), promoting the increased temperatures required for ductile deformation. Experimental deformation studies suggest that brittle failure mechanisms themselves act to increase porosity and permeability, as outlined by Violay et al. (2012). Previous work has attempted to link the BDT to a specific temperature range in Iceland, based on laboratory experiments on Icelandic basalts (550 ± 100°C—(Violay et al., 2012)) and seismicity depth limits linked to measured temperature gradients from geothermal wells on the Reykjanes Peninsula ($580 - 750$°C—(Tryggvason et al., 2002)). This temperature range has partly been confirmed by the IDDP-2 drilling in Reykjanes to a depth of 4.65 km, with estimated bottom-hole temperature in the range of 535–600°C (Bali et al., 2020; Friðleifsson et al., 2020). While other factors may affect the BDT depth (such as composition, strain rate, pore pressure and fluid saturation) a dominant temperature control is consistent with our observations of shallowing of the BDT by 1–2 km beneath the known high-temperature geothermal areas of Reykjanes, particularly Svartsengi and Krýsuvík (highlighted by brown lines at top of Figure 9b), and also observed by Flóvenz et al. (2022).

A significant feature of the Greenfield et al. (2022) seismic catalog is the observation of a tight cluster of deep low-frequency seismicity at ∼10–12 km depth beneath the BDT, which was active preceding and during the initial 2021 eruption at Fagradalsfjall (events in cyan, Figure 9). The authors hypothesize that seismicity could be caused by: (a) a structural barrier or rheological change at this depth, inhibiting magma ascent through the lower crust increasing strain rates to allow brittle failure, or (b) CO_2-rich fluids from degassing magma due to bubbles or movement through a fracture system. Within the context of crustal velocity structure, we note that this depth is consistent with discontinuity D2 (Figure 9b), which we interpret as a transition into deep crustal cumulates, potentially providing the rheological change postulated by Greenfield et al. (2022).

5.7.2. Magma Sources

Geochemical analysis of erupted products from the recent 2021–23 Fagradalsfjall eruptions showed more depleted melts that smoothly shifted to enriched primitive melts over the course of a few weeks. These have been interpreted as initial lower-degree partial melts moving directly from a relatively depleted near-Moho magma chamber (>15 km), which were swiftly replenished by more enriched deeper sourced melts, which thermobarometry indicates come from 19 to 20 km (Halldórsson et al., 2022). This is consistent with our results, which suggest a 15 km deep Moho beneath Fagrdalsfjall, and the interpretation of an underlying partially molten crust-mantle transition zone mixture, including some solidified lenses of gabbro, as described in Section 5.3.

Recent seismic tomography images produced by Troll et al. (2024) using local seismicity, show a region of high V_P/V_S ratio at 9–12 km depth beneath the Fagradalsfjall eruption site. The authors suggest this could represent a mid-crustal magma chamber that fed both the Fagradalsfjall and later Sundhnúkar eruptions. We see no corresponding low V_S anomaly in the same area of our model. While data included in our study are only sensitive to V_S, inclusion of teleseismic waves that sample the whole crust provide good sensitivity at depth compared to the Troll et al. (2024) model which is restricted to using the limited number of earthquakes occurring beneath the BDT. The lateral resolution of our model is controlled by the frequency of teleseismic data used and our approach of smoothing across the Fresnel zone of rays, which are calculated to have a diameter of ∼8–9 km at 10 km depth. Thus our model would be capable of resolving the at least 10 km wide anomaly described by Troll et al. (2024). We also note that a 10 km deep magma chamber beneath Fagradalsfjall appears inconsistent with the deep (∼19 km) thermobarometry results previously discussed (Halldórsson et al., 2022).

10.1029/2024GC011817

Matthews et al. (2024) conducted petrological analysis (clinopyroxene liquid barometery and OPAM) of erupted products from the recent 2023–24 Grindavík/Sundhnúkar eruptions, which indicate magma storage depths of ∼5.5 ± 5 km (see details in Supplementary Text S4 in Supporting Information S1), Figure 9. This is consistent with surface deformation observed in InSAR data prior to the eruptions (modeled magma source at ∼5 km depth (Sigmundsson et al., 2024)), and with predictions of magma storage depths estimated for historical eruptions from the same volcanic system (∼7 km at Svartsengi (Caracciolo et al., 2023)). In our model this depth correlates with the base of the seismically defined upper-crust (Figure 9c). This is in-line with estimates of magma storage depths observed across the majority of the Peninsula during the last rifting episode (Caracciolo et al., 2023), suggesting that magma is usually sourced from mid-crustal magma chambers on the Reykjanes Peninsula, and less frequently directly from the mantle as seen at the 2021–23 Fagradalsfjall eruptions.

6. Conclusion

We generate a new crustal shear-wave velocity model extending the full length of the Reykjanes Peninsula in SW Iceland, derived from teleseismic receiver functions and surface wave dispersion measurements. This expands both the lateral and depth coverage of crustal imaging in this region compared to previous work, improving understanding of crustal structure and providing context for the ongoing volcanic and seismic unrest the region has experienced since 2020. Conclusions that we draw from our model are summarized in Figure 8, and outlined below.

- The upper-crust is defined by sharply increasing velocity gradients to depths of 4–6 km, and is split into fractured, extrusive dominated material above 3 km and more intact, intrusive dominated material below. High-temperature geothermal systems extend throughout the upper-crust, though they transition from being characterized by fast seismic anomalies <3 km (representing mineral precipitation in fractured material), to slow anomalies >3 km (representing high-temperature systems in more intact material). The bulk of local seismicity is limited to the upper-crust.
- The lower crust is likely formed of gabbros. At 10 km a seismic discontinuity denotes a transition into a cumulate dominated lower-most crust, which is notably higher in velocity at the western end of the Peninsula and just off-shore, where it masks underlying Moho arrivals. Deep seismicity (10–12 km) linked to the 2021 Fagradalsfjall eruption is coincident with this rheological change into a cumulate dominated lowermost crust.
- Crustal thickness increases eastwards along the Peninsula from ∼15–20 km, likely due to a combination of increasing mantle potential temperatures and active upwelling moving closer to the center of the hotspot underlying central Iceland.
- Beneath the Moho to depths of 25 km, seismic velocities increase from 3.9 to 4.2 km/s, indicating a partially molten transitional zone into the underlying depleted mantle.
- The majority of historic eruptions along the Peninsula are linked with magma stored toward the top of the lower crust, similar to initial estimates from the ongoing 2023–24 Grindavík/Sundhnúkar eruptions. In contrast magma from the 2021–23 Fagradalsfjall eruption was sourced from within the partially molten crust-mantle transition zone below the 15 km deep Moho, similar to historic eruptions of the Brennisteinsfjöll volcanic system. Recent long-wavelengths correlations of shallowing magma storage with increasing crustal thickness in Iceland and off-shore along the Reykjanes Ridge do not appear to persist along the complex transtentional rift of the Reykjanes Peninsula.

Data Availability Statement

Full information on continuous waveform data used to calculate RFs and dispersion derived products in this study can be found in the supplementary material, Table S1 in Supporting Information S1. The majority of utilized seismic networks (as previously referenced in main text) are available through open-source data centers as follows: COSESMIQ 2C—Swiss Seismological Service (SED), IMAGE 4L and MAGIC 9H—GEOFON, Carnegie 3A IRIS, SIL VI ORFEUS/SED. The Cambridge University network RK is embargoed until 2025, when it will be made publicly available on IRIS via the UK Research and Innovation, Geophysical Equipment Facility SEIS-UK (Brisbourne, 2012). The REYKJANET 7E network is owned and managed by the Czech Academy of Science and Iceland Geosurvey with data access negotiations managed via ISOR. All derived seismic products are available from (Jenkins, 2024).

Acknowledgments

The authors would like to highlight the excellent attitude towards data sharing between international research groups that allowed this work to take place, along with the open source data provided by IRIS/GEOFON/ORFEUS and SED web services. The University of Cambridge network was supported by NERC Urgency grant NE/W004690/1. The Reykjanet seismic network (7E) was partially funded by the NASPMON project (NAtural Seismicity as a Prospecting and MONitoring tool for geothermal energy extraction) benefiting from a €1,370,000 grant from Iceland, Liechtenstein and Norway through the EEA Grants and the Technology Agency of the Czech Republic within the KAPPA Programme. We acknowledge useful discussions with Dr. Edward Marshall, Dr. Rachel Baxter, Dr. Alberto Carracciolo and Dr. Simon Matthews which helped shape the discussion section. This work benefited from constructive reviewers from Dr. Finn Isley-Kemp and one anonymous reviewer. Figures are produced with matplotlib and GMT6 (Wessel et al., 2019) and the obspy pygmt library (Uieda et al., 2021).

References

Allen, R. M., Nolet, G., Morgan, W. J., Vogfjörd, K., Bergsson, B. H., Erlendsson, P., et al. (2002). Imaging the mantle beneath Iceland using integrated seismological techniques. *Journal of Geophysical Research*, *107*(B12), ESE–3. https://doi.org/10.1029/2001jb000595

Árnason, K., Eysteinsson, H., & Hersir, G. P. (2010). Joint 1d inversion of TEM and MT data and 3D inversion of MT data in the Hengill Area, Sw Iceland. *Geothermics*, *39*(1), 13–34. https://doi.org/10.1016/j.geothermics.2010.01.002

Bacon, C. A., Johnson, J. H., White, R. S., & Rawlinson, N. (2022). On the origin of seismic anisotropy in the shallow crust of the Northern Volcanic Zone, Iceland. *Journal of Geophysical Research: Solid Earth*, *127*(1), e2021JB022655. https://doi.org/10.1029/2021jb022655

Bali, E., Aradi, L. E., Zierenberg, R., Diamond, L. W., Pettke, T., Szabó, Á., et al. (2020). Geothermal energy and ore-forming potential of 600 c mid-ocean-ridge hydrothermal fluids. *Geology*, *48*(12), 1221–1225. https://doi.org/10.1130/g47791.1

Baxter, R., & Maclennan, J. (2024). Influence of magma flux on magma storage depths along the Reykjanes ridge. *Earth and Planetary Science Letters*, *631*, 118633. https://doi.org/10.1016/j.epsl.2024.118633

Baxter, R., Maclennan, J., Neave, D., & Thordarson, T. (2023). Depth of magma storage under Iceland controlled by magma fluxes. *Geochemistry, Geophysics, Geosystems*, *24*(7), e2022GC010811. https://doi.org/10.1029/2022gc010811

Bird, P. (2003). An updated digital model of plate boundaries. *Geochemistry, Geophysics, Geosystems*, *4*(3), 1027. https://doi.org/10.1029/2001gc000252

Bjarnason, I. T., Menke, W., Flóvenz, Ó. G., & Caress, D. (1993). Tomographic image of the mid-Atlantic plate boundary in southwestern Iceland. *Journal of Geophysical Research*, *98*(B4), 6607–6622. https://doi.org/10.1029/92jb02412

Boudier, F., & Nicolas, A. (1995). Nature of the moho transition zone in the Oman ophiolite. *Journal of Petrology*, *36*(3), 777–796. https://doi.org/10.1093/petrology/36.3.777

Brisbourne, A. (2012). How to store and share geophysical data. *Astronomy and Geophysics*, *53*(4), 4.19–4.20. https://doi.org/10.1111/j.1468-4004.2012.53419.x

Cannat, M. (1996). How thick is the magmatic crust at slow spreading oceanic ridges? *Journal of Geophysical Research*, *101*(B2), 2847–2857. https://doi.org/10.1029/95jb03116

Caracciolo, A., Bali, E., Halldórsson, S., Guðfinnsson, G., Kahl, M., Þórðardóttir, I., et al. (2023). Magma plumbing architectures and timescales of magmatic processes during historical magmatism on the Reykjanes Peninsula, Iceland. *Earth and Planetary Science Letters*, *621*, 118378. https://doi.org/10.1016/j.epsl.2023.118378

Cottaar, S., Pugh, S., Boyce, A., & Jenkins, J. (2020). sannecottaar/smurfpy: Smurfpy. *Zenodo*. https://doi.org/10.5281/zenodo.4337258

Dahm, T., Jousset, P., Heimann, S., Milkereit, C., Hersir, G. P., & Magnússon, R. (2020). Magic - Seismic network magma in Iceland. *GFZ Data Services*. https://doi.org/10.14470/4U7575229166

DeMets, C., Gordon, R. G., & Argus, D. F. (2010). Geologically current plate motions. *Geophysical Journal International*, *181*(1), 1–80. https://doi.org/10.1111/j.1365-246x.2009.04491.x

De Pascale, G. P., Fischer, T. J., Moreland, W. M., Geirsson, H., Hrubcová, P., Drouin, V., et al. (2024). On the move: 2023 observations on real time Graben formation, Grindavík, Iceland. *Geophysical Research Letters*, *51*(14), e2024GL110150. https://doi.org/10.1029/2024gl110150

Dreiling, J., & Tilmann, F. (2019). Bayhunter - Mcmc transdimensional bayesian inversion of receiver functions and surface wave dispersion. *GFZ Data Services*. https://doi.org/10.5880/GFZ.2.4.2019.001

Du, Z., Foulger, G., Julian, B., Allen, R., Nolet, G., Morgan, W., et al. (2002). Crustal structure beneath western and eastern Iceland from surface waves and receiver functions. *Geophysical Journal International*, *149*(2), 349–363. https://doi.org/10.1046/j.1365-246x.2002.01642.x

Einarsson, P., Eyjólfsson, V., & Hjartardóttir, Á. R. (2023). Tectonic framework and fault structures in the Fagradalsfjall segment of the Reykjanes Peninsula Oblique Rift, Iceland. *Bulletin of Volcanology*, *85*(2), 9. https://doi.org/10.1007/s00445-022-01624-x

Ekström, G., Abers, G. A., & Webb, S. C. (2009). Determination of surface-wave phase velocities across USArray from noise and Aki's spectral formulation. *Geophysical Research Letters*, *36*(18), L18301. https://doi.org/10.1029/2009gl039131

Fischer, T., Hrubcová, P., Salama, A., Doubravová, J., Agústsdóttir, T., Gudnason, E., et al. (2022). Swarm seismicity illuminates stress transfer prior to the 2021 Fagradalsfjall eruption in Iceland. *Earth and Planetary Science Letters*, *594*, 117685. https://doi.org/10.1016/j.epsl.2022.117685

Flóvenz, Ó. G., & Gunnarsson, K. (1991). Seismic crustal structure in Iceland and surrounding area. *Tectonophysics*, *189*(1–4), 1–17. https://doi.org/10.1016/0040-1951(91)90483-9

Flóvenz, Ó. G., Wang, R., Hersir, G. P., Dahm, T., Hainzl, S., Vassileva, M., et al. (2022). Cyclical geothermal unrest as a precursor to Iceland's 2021 Fagradalsfjall eruption. *Nature Geoscience*, *15*(5), 397–404. https://doi.org/10.1038/s41561-022-00930-5

Franzson, H., Gunnlaugsson, E., Árnason, K., Sæmundsson, K., Steingrímsson, B., & Hardarson, B. (2010). The Hengill geothermal system, conceptual model and thermal evolution. *Proceedings world geothermal congress*, *25*, 1.

Friðleifsson, G. Ó., Elders, W. A., Zierenberg, R. A., Fowler, A. P., Weisenberger, T. B., Mesfin, K. G., et al. (2020). The Iceland deep drilling project at Reykjanes: Drilling into the root zone of a black smoker analog. *Journal of Volcanology and Geothermal Research*, *391*, 106435. https://doi.org/10.1016/j.jvolgeores.2018.08.013

Friðleifsson, G. Ó., Elders, W. A., Zierenberg, R. A., Stefánsson, A., Fowler, A. P., Weisenberger, T. B., et al. (2017). The Iceland Deep Drilling Project 4.5 km deep well, IDDP-2, in the seawater-recharged reykjanes geothermal field in SW Iceland has successfully reached its supercritical target. *Scientific Drilling*, *23*, 1–12. https://doi.org/10.5194/sd-23-1-2017

Gasperikova, E., Rosenkjaer, G. K., Arnason, K., Newman, G. A., & Lindsey, N. J. (2015). Resistivity characterization of the Krafla and Hengill geothermal fields through 3d MT inverse modeling. *Geothermics*, *57*, 246–257. https://doi.org/10.1016/j.geothermics.2015.06.015

Gilligan, A., Priestley, K. F., Roecker, S. W., Levin, V., & Rai, S. (2015). The crustal structure of the western Himalayas and Tibet. *Journal of Geophysical Research: Solid Earth*, *120*(5), 3946–3964. https://doi.org/10.1002/2015jb011891

Greenfield, T., Winder, T., Rawlinson, N., Maclennan, J., White, R. S., Ágústsdóttir, T., et al. (2022). Deep long period seismicity preceding and during the 2021 Fagradalsfjall eruption, Iceland. *Bulletin of Volcanology*, *84*(12), 101. https://doi.org/10.1007/s00445-022-01603-2

Grigoli, F., Clinton, J. F., Diehl, T., Kaestli, P., Scarabello, L., Agustsdottir, T., et al. (2022). Monitoring microseismicity of the Hengill geothermal field in Iceland. *Scientific Data*, *9*(1), 220. https://doi.org/10.1038/s41597-022-01339-w

Halldórsson, S. A., Marshall, E. W., Caracciolo, A., Matthews, S., Bali, E., Rasmussen, M. B., et al. (2022). Rapid shifting of a deep magmatic source at Fagradalsfjall volcano, Iceland. *Nature*, *609*(7927), 529–534. https://doi.org/10.1038/s41586-022-04981-x

Harmon, N., & Rychert, C. A. (2016). Joint inversion of teleseismic and ambient noise Rayleigh waves for phase velocity maps, an application to Iceland. *Journal of Geophysical Research: Solid Earth*, *121*(8), 5966–5987. https://doi.org/10.1002/2016jb012934

Harðarson, B. S., Fitton, J. G., & Hjartarson, Á. (2008). Tertiary volcanism in Iceland. *Jökull Journal*, *58*(1), 161–178. https://doi.org/10.33799/jokull2008.58.161

Herrmann, R. B. (2013). Computer programs in seismology: An evolving tool for instruction and research. *Seismological Research Letters*, *84*(6), 1081–1088. https://doi.org/10.1785/0220110096

Hersir, G. P., Árnason, K., Vilhjálmsson, A. M., Saemundsson, K., Ágústsdóttir, Þ., & Friðleifsson, G. Ó. (2020). Krỳsuvík high temperature geothermal area in SW Iceland: Geological setting and 3D inversion of magnetotelluric (MT) resistivity data. *Journal of Volcanology and Geothermal Research*, *391*, 106500. https://doi.org/10.1016/j.jvolgeores.2018.11.021

Icelandic Meteorological Office. (1992). Icelandic national digital seismograph network. *International Federation of Digital Seismograph Networks*. https://doi.org/10.7914/ZKJM-TJ71

Ito, G., Shen, Y., Hirth, G., & Wolfe, C. J. (1999). Mantle flow, melting, and dehydration of the Iceland mantle plume. *Earth and Planetary Science Letters*, *165*(1), 81–96. https://doi.org/10.1016/s0012-821x(98)00216-7

Jenkins, J. (2017). The seismic signature of the Iceland mantle plume from crust to mid-mantle. PhD Dissertation.

Jenkins, J. (2024). Derived seismic data products from paper: "seismic imaging of the reykjanes peninsular, Iceland: Crustal-scale context of geothermal areas and ongoing volcano-tectonic unrest [Dataset]. *Zenodo*. https://doi.org/10.5281/zenodo.13235058

Josef Horalek. (2013). Reykjanet. *International Federation of Digital Seismograph Networks*. https://doi.org/10.7914/SN/7E_2013

Jousset, P., Blanck, H., Hersir, G. P., Kirk, H., Erbas, K., Ágústsson, K., et al. (2020). Image (integrated methods for advanced geothermal exploration). *GFZ Data Services*. https://doi.org/10.14470/9Y7569325908

Karlsdóttir, R., Vilhjálmsson, A. M., & Guðnason, E. Á. (2020). Three dimensional inversion of magnetotelluric (MT) resistivity data from Reykjanes high temperature field in SW Iceland. *Journal of Volcanology and Geothermal Research*, *391*, 106498. https://doi.org/10.1016/j.jvolgeores.2018.11.019

Kästle, E. D., Soomro, R., Weemstra, C., Boschi, L., & Meier, T. (2016). Two-receiver measurements of phase velocity: Cross-validation of ambient-noise and earthquake-based observations. *Geophysical Journal International*, *207*(3), 1493–1512. https://doi.org/10.1093/gji/ggw341

Keiding, M., Lund, B., & Árnadóttir, T. (2009). Earthquakes, stress, and strain along an obliquely divergent plate boundary: Reykjanes peninsula, southwest Iceland. *Journal of Geophysical Research*, *114*(B9), B09306. https://doi.org/10.1029/2008jb006253

Kelemen, P. B., & Holbrook, W. S. (1995). Origin of thick, high-velocity igneous crust along the us east coast margin. *Journal of Geophysical Research*, *100*(B6), 10077–10094. https://doi.org/10.1029/95jb00924

Kind, R., Yuan, X., Saul, J., Nelson, D., Sobolev, S., Mechie, J., et al. (2002). Seismic images of crust and upper mantle beneath Tibet: Evidence for Eurasian plate subduction. *Science*, *298*(5596), 1219–1221. https://doi.org/10.1126/science.1078115

Korenaga, J., & Kelemen, P. B. (1997). Origin of gabbro sills in the Moho transition zone of the Oman ophiolite: Implications for magma transport in the oceanic lower crust. *Journal of Geophysical Research*, *102*(B12), 27729–27749. https://doi.org/10.1029/97jb02604

Lecocq, T., Caudron, C., & Brenguier, F. (2014). MSNoise, a python package for monitoring seismic velocity changes using ambient seismic noise. *Seismological Research Letters*, *85*(3), 715–726. https://doi.org/10.1785/0220130073

Ligorría, J. P., & Ammon, C. J. (1999). Iterative deconvolution and receiver-function estimation. *Bulletin of the Seismological Society of America*, *89*(5), 1395–1400. https://doi.org/10.1785/bssa0890051395

Maclennan, J., McKenzie, D., & Gronvöld, K. (2001). Plume-driven upwelling under central Iceland. *Earth and Planetary Science Letters*, *194*(1–2), 67–82. https://doi.org/10.1016/s0012-821x(01)00553-2

Málek, J., Brokešová, J., & Novotnỳ, O. (2019). Seismic structure beneath the Reykjanes Peninsula, southwest Iceland, inferred from array-derived Rayleigh wave dispersion. *Tectonophysics*, *753*, 1–14. https://doi.org/10.1016/j.tecto.2018.12.020

Matthews, S., Caracciolo, A., Bali, E., Halldórsson, S. A., Sigmarsson, O., Guðfinnsson, G. H., et al. (2024). A dynamic mid-crustal magma domain revealed by the 2023 to 2024 sundhnúksgígar eruptions in Iceland. *Science*, *386*(6719), 309–314. https://doi.org/10.1126/science.adp8778

Matthews, S., Wong, K., Shorttle, O., Edmonds, M., & Maclennan, J. (2021). Do olivine crystallization temperatures faithfully record mantle temperature variability? *Geochemistry, Geophysics, Geosystems*, *22*(4), e2020GC009157. https://doi.org/10.1029/2020gc009157

Mielke, P., Bär, K., & Sass, I. (2017). Determining the relationship of thermal conductivity and compressional wave velocity of common rock types as a basis for reservoir characterization. *Journal of Applied Geophysics*, *140*, 135–144. https://doi.org/10.1016/j.jappgeo.2017.04.002

Obermann, A., & Ágústsdóttir, T., & Swiss Seismological Service (SED) at ETH Zurich. (2018). Coseismiq - Control seismicity and manage induced earthquakes. *ETH Zurich*. Retrieved from http://networks.seismo.ethz.ch/networks/2c/doi:10.12686/SED/NETWORKS/2C

Obermann, A., Wu, S.-M., Ágústsdóttir, T., Duran, A., Diehl, T., Sánchez-Pastor, P., et al. (2022). Seismicity and 3-d body-wave velocity models across the Hengill geothermal area, SW Iceland. *Frontiers in Earth Science*, *10*, 969836. https://doi.org/10.3389/feart.2022.969836

Parkin, C., & White, R. (2008). Influence of the Iceland mantle plume on oceanic crust generation in the North Atlantic. *Geophysical Journal International*, *173*(1), 168–188. https://doi.org/10.1111/j.1365-246x.2007.03689.x

Parks, M., Sigmundsson, F., Drouin, V., Hjartardóttir, Á. R., Geirsson, H., Hooper, A., et al. (2023). Deformation, seismicity, and monitoring response preceding and during the 2022 Fagradalsfjall eruption, Iceland. *Bulletin of Volcanology*, *85*(10), 60. https://doi.org/10.1007/s00445-023-01671-y

Pedersen, G., Belart, J., Óskarsson, B. V., Gunnarson, S. R., Gudmundsson, M. T., Reynolds, H. I., et al. (2024). Volume, effusion rates and lava hazards of the 2021, 2022 and 2023 Reykjanes fires: Lessons learned from near real-time photogrammetric monitoring. In *Egu general assembly conference abstracts*.10724

Pugh, S., Jenkins, J., Boyce, A., & Cottaar, S. (2021). Global receiver function observations of the x-discontinuity reveal recycled basalt beneath hotspots. *Earth and Planetary Science Letters*, *561*, 116813. https://doi.org/10.1016/j.epsl.2021.116813

Rahimi Dalkhani, A., Ágústsdóttir, T., Gudnason, E. A., Hersir, G. P., Zhang, X., & Weemstra, C. (2024). Transdimensional ambient-noise surface wave tomography of the Reykjanes Peninsula, SW Iceland. *Geophysical Journal International*, *236*(1), 621–643. https://doi.org/10.1093/gji/ggad435

Rawlinson, N., & Sambridge, M. (2005). The fast marching method: An effective tool for tomographic imaging and tracking multiple phases in complex layered media. *Exploration Geophysics*, *36*(4), 341–350. https://doi.org/10.1071/eg05341

Sæmundsson, K., Sigurgeirsson, M. Á., & Friðleifsson, G. Ó. (2020). Geology and structure of the Reykjanes volcanic system, Iceland. *Journal of Volcanology and Geothermal Research*, *391*, 106501. https://doi.org/10.1016/j.jvolgeores.2018.11.022

Sánchez-Pastor, P., Obermann, A., Reinsch, T., Ágústsdóttir, T., Gunnarsson, G., Tómasdóttir, S., et al. (2021). Imaging high-temperature geothermal reservoirs with ambient seismic noise tomography, a case study of the Hengill geothermal field, SW Iceland. *Geothermics*, *96*, 102207. https://doi.org/10.1016/j.geothermics.2021.102207

Shorttle, O., Maclennan, J., & Piotrowski, A. M. (2013). Geochemical provincialism in the Iceland plume. *Geochimica et Cosmochimica Acta*, *122*, 363–397. https://doi.org/10.1016/j.gca.2013.08.032

Sigmundsson, F., Einarsson, P., Hjartardóttir, Á. R., Drouin, V., Jónsdóttir, K., Arnadottir, T., et al. (2020). Geodynamics of Iceland and the signatures of plate spreading. *Journal of Volcanology and Geothermal Research*, *391*, 106436. https://doi.org/10.1016/j.jvolgeores.2018.08.014

Sigmundsson, F., Parks, M., Geirsson, H., Hooper, A., Drouin, V., Vogfjörd, K. S., et al. (2024). Fracturing and tectonic stress drive ultrarapid magma flow into dikes. *Science*, *383*(6688), 1228–1235. https://doi.org/10.1126/science.adn2838

Sigmundsson, F., Parks, M., Hooper, A., Geirsson, H., Vogfjörd, K. S., Drouin, V., et al. (2022). Deformation and seismicity decline before the 2021 Fagradalsfjall eruption. *Nature*, *609*(7927), 523–528. https://doi.org/10.1038/s41586-022-05083-4

Smallwood, J. R., & White, R. S. (1998). Crustal accretion at the Reykjanes ridge, 61–62 n. *Journal of Geophysical Research*, *103*(B3), 5185–5201. https://doi.org/10.1029/97jb03387

Troll, V. R., Deegan, F. M., Thordarson, T., Tryggvason, A., Krmíček, L., Moreland, W. M., et al. (2024). The fagradalsfjall and sundhnúkur fires of 2021–2024: A single magma reservoir under the reykjanes peninsula, Iceland? *Terra Nova*, *36*(6), 447–456. https://doi.org/10.1111/ter.12733

Tryggvason, A., Rögnvaldsson, S. T., & Flóvenz, O. G. (2002). Three-dimensional imaging of the P-and S-wave velocity structure and earthquake locations beneath Southwest Iceland. *Geophysical Journal International*, *151*(3), 848–866. https://doi.org/10.1046/j.1365-246x.2002.01812.x

Uieda, L., Tian, D., Leong, W. J., Toney, L., Schlitzer, W., Grund, M., et al. (2021). PyGMT: A Python interface for the generic mapping tools.

Violay, M., Gibert, B., Mainprice, D., Evans, B., Dautria, J.-M., Azais, P., & Pezard, P. (2012). An experimental study of the brittle-ductile transition of basalt at oceanic crust pressure and temperature conditions. *Journal of Geophysical Research*, *117*(B3), B03213. https://doi.org/10.1029/2011jb008884

Volk, O. (2021). Velocity and anisotropy structure of the Icelandic crust-an ambient seismic noise analysis. PhD Dissertation.

Weir, N. R., White, R. S., Brandsdóttir, B., Einarsson, P., Shimamura, H., & Shiobara, H. (2001). Crustal structure of the northern Reykjanes Ridge and Reykjanes Peninsula, southwest Iceland. *Journal of Geophysical Research*, *106*(B4), 6347–6368. https://doi.org/10.1029/2000jb900358

Wessel, P., Luis, J. F., Uieda, L. a., Scharroo, R., Wobbe, F., Smith, W. H., & Tian, D. (2019). The generic mapping tools version 6. *Geochemistry, Geophysics, Geosystems*, *20*(11), 5556–5564. https://doi.org/10.1029/2019gc008515

Wu, S.-M., Sánchez-Pastor, P., Ágústsdóttir, T., Hersir, G. P., Mordret, A., Hjörleifsdóttir, V., & Obermann, A. (2024). Crustal characterization of the Hengill geothermal fields: Insights from isotropic and anisotropic seismic noise imaging using a 500-node array. *Journal of Geophysical Research: Solid Earth*, *129*(7), e2024JB028915. https://doi.org/10.1029/2024jb028915